



Kent Academic Repository

Gu, Mengtao, Xu, Chuanlong, Hossain, Md. Moinul and Li, Jian (2023) A low-rank decomposition-based deconvolution algorithm for rapid volumetric reconstruction of light field PIV. A low-rank decomposition-based deconvolution algorithm for rapid volumetric reconstruction of light field PIV, 64 (2). ISSN 1432-1114. (In press)

Downloaded from

<https://kar.kent.ac.uk/99994/> The University of Kent's Academic Repository KAR

The version of record is available from

<https://doi.org/10.1007/s00348-023-03575-1>

This document version

Author's Accepted Manuscript

DOI for this version

Licence for this version

UNSPECIFIED

Additional information

Unmapped bibliographic data:JO - Experiments in Fluids [Field not mapped to EPrints]

Versions of research works

Versions of Record

If this version is the version of record, it is the same as the published version available on the publisher's web site. Cite as the published version.

Author Accepted Manuscripts

If this document is identified as the Author Accepted Manuscript it is the version after peer review but before type setting, copy editing or publisher branding. Cite as Surname, Initial. (Year) 'Title of article'. To be published in *Title of Journal*, Volume and issue numbers [peer-reviewed accepted version]. Available at: DOI or URL (Accessed: date).

Enquiries

If you have questions about this document contact ResearchSupport@kent.ac.uk. Please include the URL of the record in KAR. If you believe that your, or a third party's rights have been compromised through this document please see our [Take Down policy](https://www.kent.ac.uk/guides/kar-the-kent-academic-repository#policies) (available from <https://www.kent.ac.uk/guides/kar-the-kent-academic-repository#policies>).

A low-rank decomposition-based deconvolution algorithm for rapid volumetric reconstruction of light field μ PIV

Mengtao Gu,^a Jian Li,^{*a} Md. Moinul Hossain,^b and Chuanlong Xu^{*a}

Received 00th January 20xx,
Accepted 00th January 20xx

DOI: 10.1039/x0xx00000x

Light field micro-particle image velocimetry (LF- μ PIV) can characterize three-dimensional (3-D) microflow through the volumetric reconstruction of tracer particle distributions. This can be achieved by light field imaging and volumetric reconstruction techniques such as the Richardson-Lucy deconvolution (RLD) method. However, the convolution operations of RLD are computationally complex due to the laterally shift-variant point spread function (PSF), which significantly lowers the reconstruction efficiency. Thus, a low-rank decomposition-based deconvolution (LRDD) method is proposed to improve the reconstruction efficiency. Through direct deconvolution, the PSF is converted to a point source, eliminating the shift variance and decreasing the number of convolution kernels, thereby reducing the computational complexity of convolution operations. Further, the point source, which is composed of several two-dimensional (2-D) matrices, is decomposed into one-dimensional (1-D) kernels through low-rank decomposition for reducing the computational time of convolution operations. The performance of LRDD and RLD is investigated by numerical studies on the volumetric reconstruction. Experiments were carried out in a microchannel to validate the proposed LRDD. Results demonstrated that the reconstruction efficiency of LRDD is above 9 times faster than RLD for the volumetric reconstruction of the tracer particle distribution.

1 Introduction

Microfluidic chips are widely used in biological, chemical and environmental fields due to the advantages of high integration, low reagent consumption and strong controllability¹⁻³. The performance of microfluidic chips such as micro-mixers and micro-reactors is closely related to the flow state of the internal microfluid. The convective, secondary and vortex flow in the microchannel can increase the contact area of different microfluid and thus improve the mixing or reaction performance of microfluidic chips^{4,5}. Therefore, three-dimensional (3-D) measurement and characterization of the microflow is of great significance for the design and optimization of microfluidic chips⁶.

Light field (LF) imaging technique can capture the four-dimensional (4-D) information (i.e., 2-D lateral position and 2-D angular information) of a scene within a single camera frame^{7,8}. The 3-D reconstruction of the scene can be realized with the axial depth of the scene derived from the angular information⁹⁻¹³. Recently, LF micro-particle image velocimetry (LF- μ PIV)^{14,15} has been developed based on LF imaging and μ PIV techniques. With the integration of a microlens array (MLA) between the microscope tube lens and the camera¹⁶, the LF microscope can record the 3-D tracer particle

distribution in microflow in a single exposure. As a result, LF- μ PIV can measure the instantaneous 3-D velocity field of microflow through a single camera. Also, the LF- μ PIV has apparent advantages in simplifying the experimental system and improving the temporal resolution, which overcomes the shortcomings of the conventional 3-D μ PIV techniques, such as the low temporal resolution in confocal μ PIV¹⁷, and the complexity of the imaging system in holographic μ PIV¹⁸. Therefore, in recent years, the LF- μ PIV has become one of the research interests in microfluidic measurement techniques.

The LF- μ PIV reconstructs the tracer particle distributions through LF images and a volumetric reconstruction technique. Consequently, the 3-D velocity field of microflow can be achieved by the cross-correlation calculation of the two consecutive reconstructed tracer particle distributions^{14,15}. Thus, the development of a rapid and accurate volumetric reconstruction technique is crucial for LF- μ PIV to realize the microflow's 3-D velocity field measurement precisely. Data-driven and model-based approaches are used for the volumetric reconstruction of the tracer particle distribution¹⁹. The data-driven approach establishes a prediction model based on the mapping between LF images and corresponding 3-D scenes through deep learning technique¹⁹. Studies^{20,21} adapted a U-net architecture to establish a prediction model and LF images of particles and the corresponding 3-D particle distributions are used as training data. However, a large number of high-resolution 3-D particle distribution data is needed for the training and optimization of the prediction model. Thus, additional high-resolution 3-D imaging devices

^a National Engineering Research Center of Power Generation Control and Safety, School of Energy and Environment, Southeast University, Nanjing, China. E-mail: chuanlongxu@seu.edu.cn; eelijian@seu.edu.cn

^b School of Engineering, University of Kent, Canterbury, Kent CT2 7NT, UK.

such as confocal and light-sheet microscopes are required, which is costly and difficult to implement, thereby limiting the practical application of the data-driven approach.

In contrast to the data-driven approach, the model-based approaches realize the volumetric reconstruction of tracer particle distributions where significant data collection is not necessary. However, these model-based approaches such as Refocusing^{14,16}, ray-intersection²² and Richardson-Lucy deconvolution (RLD)^{15,23} establish a LF microscope forward imaging model based on the optics theories and then reversely carry out backward volumetric reconstruction. The reconstruction accuracy of these approaches is related to the accuracy of the forward imaging model. The refocusing and ray-intersection methods describe the ray propagation process based on geometrical optics theory and realize the volumetric reconstruction of tracer particle distribution through an inverse ray tracing technique. Although these methods take lower computational time for the volumetric reconstruction, the diffraction effect of the microscope is ignored by geometrical optics theory. The microlens is also simplified as a pinhole, i.e., only the center of the microlens is used for light sampling. Consequently, the light sampling density is limited by the microlens pitch (usually in the order of one hundred micrometers), resulting in lower lateral resolution and axial positioning accuracy of the reconstructed tracer particle^{14,15,22,23}.

The RLD method utilizes wave optics theory by considering the diffraction effect to model the point spread function (PSF), which accurately models the forward imaging process²³. In addition, wave optics theory does not assume the microlens as a pinhole, which makes the space of light sampling smaller than the microlens pitch and improves the light sampling density. As a result, the reconstructed tracer particle distribution has higher lateral resolution and axial positioning accuracy²⁴. Thus, the RLD method is one of the applicable methods for volumetric reconstruction in LF- μ PIV. However, due to the imaging effect of MLA, the PSF of the LF microscope is laterally shift-variant²³ and RLD needs to process a huge number of 2-D convolution operations during the reconstruction process which seriously lowers the reconstruction efficiency. A phase-space deconvolution is proposed to improve the reconstruction efficiency of RLD and the convergence speed based on the smoothness prior²⁵. However, the smoothness prior is only applicable to continuous objects, such as cells and biological tissues, rather than the discrete micro tracer particles. For LF- μ PIV, the forward calculation process of RLD is modified by the sparse characteristic of tracer particle distribution to eliminate the calculation redundancy caused by the zero voxels and thus to improve the reconstruction efficiency by 2-fold²⁶. However, this modified method doesn't optimize the 2-D convolution operations in the backward calculation process of RLD and takes longer computational time to complete the volumetric reconstruction²⁶. Therefore, optimizations for the complex convolution operations of RLD are needed to improve the reconstruction efficiency in LF- μ PIV.

In the RLD, the PSF on the image plane is formed by the

point source in object space through the forward imaging model. In object space, the angle of the point source related to the center of the microlens is different when the point source locates at different lateral positions, resulting in distinct PSF patterns on the image plane. As a result, the laterally shift-invariant point source in object space is converted to the laterally shift-variant PSF on the image plane after the forward imaging model^{23,26}. The forward imaging model from object space to the image plane in the LF microscope can be expressed as the direct convolution between the point source and corresponding PSF¹⁵. Direct deconvolution is the inverse operation of convolution and represents the backward reconstruction process from the image plane to object space²⁷. Thus, the point source in object space can be reconstructed from the PSF on the image plane through direct deconvolution to eliminate the lateral shift variance and to reduce the number of 2-D convolution operations. Moreover, the simplification of the 2-D convolution operation can further improve the reconstruction efficiency. The Low-rank decomposition²⁸⁻³⁰ method also simplifies the 2-D convolution operation. By decomposing the 2-D convolution kernel into two one-dimensional (1-D) ones, low-rank decomposition can significantly reduce the computational time of 2-D convolution operations. Thus, applying low-rank decomposition to deal with the 2-D convolution operations in RLD has the potential to improve the reconstruction efficiency in LF- μ PIV.

In this study, a new low-rank decomposition-based deconvolution (LRDD) method is proposed for reducing the computational time of convolution operations and improving the efficiency of the volumetric reconstruction of the tracer particle distribution in LF- μ PIV. Through direct deconvolution, the laterally shift-variant PSF in the RLD method is reconstructed into a laterally shift-invariant point source, which reduces the number of 2-D convolution operations. The low-rank decomposition is then applied to simplify the 2-D convolution operations and further improve the reconstruction efficiency. Numerical simulations were conducted on the volumetric reconstruction of tracer particle distributions to verify and compare the reconstruction efficiency of LRDD and RLD. Experiments of the microflow in a Y-shaped microchannel were also carried out to validate the performance of the proposed LRDD. The results achieved from simulations and experiments are presented and discussed.

2 Low-rank decomposition-based deconvolution

Fig. 1 shows the forward imaging model of the LF microscope. The light intensity is instantaneously recorded by the LF microscope and formed LF image. With the captured LF image, the volumetric reconstruction of the tracer particle distribution can be performed through RLD, which is expressed as,

$$F_{i+1} = \left\{ (G \oplus H_t) / [(F_i \oplus H) \oplus H_t] \right\} F_i \quad (1)$$

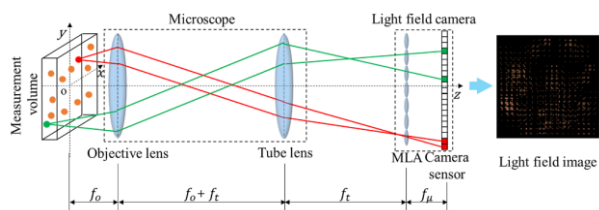


Fig. 1 Schematic diagram of the forward imaging model of the LF microscope

where F_i and F_{i+1} represent the estimation of the tracer particle distribution at the i_{th} and $(i+1)_{th}$ iteration, respectively. G is the LF image captured by the LF microscope. H is a series of PSF of the LF microscope. H_t is the transpose of H . The symbol “ \oplus ” represents the compound operation of convolution and summation. Details can be found elsewhere in the references^{26,31}.

In the RLD, the computational time mainly occurs from the generation of the intermediated particle distribution F'_i , which is expressed as,

$$F'_i = (F_i \oplus H) \oplus H_t \quad (2)$$

where F'_i needs to be updated as F_i varies with iteration. Moreover, the number of H and H_t is vast due to the lateral shift-variance of PSF²³. Assuming the ratio of the microlens pitch to the pixel pitch is N^2 , the PSFs in the whole measurement volume is N^2K ²⁶. The number of H_t is also N^2K . Hence, $2N^2K$ 2-D convolution operations need to be completed to obtain F'_i according to Eq. (2), which is time-consuming.

$$K = \frac{D_{mea}}{V_z} + 1 \quad (3)$$

where K is the number of depth layers in the measurement volume, D_{mea} and V_z represent the axial depth volume and axial voxel size of measurement, respectively.

According to the commutative law of convolution and summation, Eq. (2) can be rewritten as,

$$F'_i = F_i \oplus (H \oplus H_t) = F_i \oplus P \quad (4)$$

H records the pixel distribution of the point source by the forward imaging model, and H_t defines a backward projection of a single pixel through the LF microscope into object space³². Thus, $P = H \oplus H_t$ can be considered as the direct deconvolution of the LF image of a point light source, which represents the reconstructed point source (RPS) in object space. Comparing Eq. (4) with Eq. (2), it can be seen that the convolution kernels change from PSF and its transpose (H and H_t) to RPS (P). Notably, RPS is nonuniform along with the axial depth but shift-invariant in the lateral direction. As a result, RPS can be generated from the PSF on the optical axis and H_t for a specific depth layer, which can be expressed as,

$$P^m = H^m \oplus H_t \quad (m = 1, 2, \dots, K) \quad (5)$$

where P^m represents the RPS at m_{th} depth layer with the size

of $d \times d \times K$, and H^m is the PSF on the optical axis at m_{th} depth layer with the size of $d \times d$. d is the ratio of the lateral size of RPS to that of the voxel, which is in the order of tens. Every RPS is a 3-D convolution matrix consisting of K 2-D matrices, representing the intensity distribution of RPS at different depth layers. There are K^2 2-D component matrices as convolution kernels in P , meaning that the number of 2-D convolution operations in Eq. (4) is K^2 . As mentioned previously, $2N^2K$ 2-D convolution operations need to be performed according to Eq. (2). In LF- μ PIV, N^2 is usually in the order of hundreds, while K is usually in the order of tens^{15,24,26}. Thus, the value of K^2 is less than that of $2N^2K$, indicating that direct deconvolution can reduce the number of 2-D convolution operations.

After the direct deconvolution in Eq. (5), the K^2 2-D convolution operations in Eq. (4) can then be written as,

$$F'_i = \sum_{m=1}^K \sum_{m'=1}^K (F_i^m * P_{m'}^m) \quad (6)$$

where F_i^m represents the 2-D component matrix of F_i at m_{th} depth layer with the size of $s \times t$. The values of $s \times t$ are decided by the size of the LF image. $P_{m'}^m$ is the 2-D component matrix of P^m at m_{th} depth layer with the size of $d \times d$. The symbol “ $*$ ” represents the convolution operation.

As the RPS (P^m) can be fitted with a 3-D Gaussian distribution function²¹, the K^2 2-D convolution kernels ($P_{m'}^m$) can be approximated correspondingly as a group of low-rank 2-D Gaussian distribution matrices. According to low-rank decomposition, the 2-D low-rank convolution kernel $P_{m'}^m$ can be decomposed into two 1-D ones^{28,30}, which is expressed as,

$$P_{m'}^m \approx h_{m'}^m * v_{m'}^m \quad (m = 1, 2, \dots, K; m' = 1, 2, \dots, K) \quad (7)$$

where $h_{m'}^m$ and $v_{m'}^m$ represent the horizontal and vertical 1-D convolution kernels with the size of $d \times 1$ and $1 \times d$ respectively. Then, the 2-D convolution operation of F_i^m and $P_{m'}^m$ in Eq. (6) is transformed into

$$F_i^m * P_{m'}^m \approx (F_i^m * h_{m'}^m) * v_{m'}^m \quad (8)$$

As the sizes of F_i^m and $P_{m'}^m$ are $s \times t$ and $d \times d$ respectively, the computational time of $F_i^m * P_{m'}^m$ is $O(d^2st)$. Since the sizes of $h_{m'}^m$ and $v_{m'}^m$ are $d \times 1$ and $1 \times d$ respectively, the computational time of $(F_i^m * h_{m'}^m) * v_{m'}^m$ is $O(2dst)$ ²⁸. $O(\cdot)$ represents the asymptotic upper bound and describes the influence of input-data size on the computational time. As d is much greater than 2, low-rank decomposition reduces the computational time of the convolution operation significantly.

The calculation of F'_i through low-rank decomposition can be expressed as,

$$F'_i \approx \sum_{m=1}^K \sum_{m'=1}^K (F_i^m * h_{m'}^m) * v_{m'}^m \quad (9)$$

The total computational time of Eq. (9) is $O(2K^2dst)$, while that of Eq. (2) is $O(2N^2Kd^2st)$. In theory, the reconstruction is

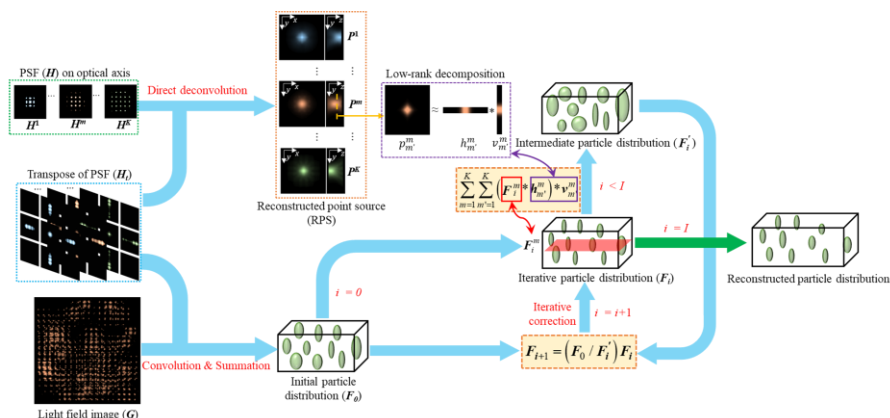


Fig. 2 Schematic diagram of proposed low-rank decomposition-based deconvolution

accelerated by the times of N^2d/K . Therefore, low-rank decomposition can improve the efficiency of the volumetric reconstruction significantly.

By substituting Eq. (9) into Eq. (1), the low-rank decomposition-based deconvolution (LRDD) can be written as,

$$F_{i+1} = \left\{ (G \oplus H_t) / \left[\sum_{m=1}^K \sum_{m'=1}^K (F_i^m * h_{m'}^m) * v_{m'}^m \right] \right\} F_i \quad (10)$$

Comparing Eq. (10) with Eq. (1), the convolution kernels change from 2-D kernels (H and H_t) to 1-D kernels ($h_{m'}^m$ and $v_{m'}^m$) through low-rank decomposition during the generation of the intermediated particle distribution F_i' in each iteration, which significantly reduces the computational time of the convolution operations. As a result, LRDD substantially improves the reconstruction efficiency since the calculation of F_i' accounts for most of the computational time of the iterative reconstruction.

Fig. 2 illustrates the schematic diagram for the volumetric reconstruction of the tracer particle distribution with the proposed LRDD. The PSF on the optical axis is converted to the RPS through direct deconvolution. Then, low-rank decomposition is performed on the RPS to acquire the 1-D convolution kernels. The initial particle distribution F_0 is obtained through the LF image G and the transpose of PSF H_t . The iterative correction is then implemented to optimize the particle distribution. For each correction, the intermediated particle distribution F_i' is acquired by convoluting the iterative particle distribution F_i with the 1-D convolution kernels obtained by low-rank decomposition. The reconstruction stops when the maximum number of iterations (I) is reached.

3 Numerical simulations

Numerical simulations were carried out to evaluate the performance of LRDD by reconstructing the volumetric particle distribution in the measurement volume. Fig. 3 illustrates the procedure of the simulations. The measurement volume is placed in the region of $30 \mu\text{m} \leq z \leq 130 \mu\text{m}$ and divided into 650×500 voxels in the lateral direction. z represents the axial

depth and the section of $z = 0$ is the focal plane of the objective lens. The PSF and the original particle distribution synthesize the LF image. For a comparative analysis, the reconstructed particle distributions are obtained from the synthetic image through RLD and LRDD. The reconstruction is performed on an Intel Core i9-10940X processor with a memory of 128 Gbytes. The optical parameters of the LF microscope are listed in Table 1.

Two different criteria such as the reconstruction quality³³ and correlation quality³⁴ are used to assess the quality of the volumetric reconstruction. The reconstruction quality Q is defined to evaluate the reconstruction accuracy of the particle distribution³³ and expressed as

$$Q = \frac{\sum E_O(x, y, z) E_R(x, y, z)}{\sqrt{\sum E_O^2(x, y, z) \sum E_R^2(x, y, z)}} \quad (11)$$

where $E_O(x, y, z)$ is the original particle distribution, and $E_R(x, y, z)$ is the reconstructed one. Q ranges from 0 to 1, and a larger Q represents a higher reconstruction performance.

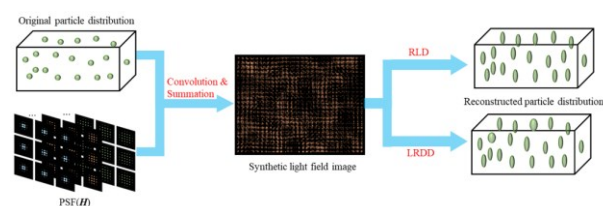


Fig. 3 Procedure of numerical simulation

Table 1 Optical Parameters of LF Microscope

Elements	Parameters	Values
Objective lens	Magnification (M_m)	10
	Numerical aperture (NA)	0.3
Microlens array	Microlens pitch (D)	137.5 μm
	Focal length (f_μ)	2292 μm
Camera	Pixel pitch (P_p)	5.5 μm

Though the reconstruction quality Q can describe the similarity between the reconstructed particle distribution and the original one, other such as the correlation quality is more critical for PIV purposes. The correlation quality³⁴ evaluates the accuracy of cross-correlation results and is defined as,

$$C = \frac{1}{N_V} \sum_{i=1}^{N_V} |v_{R,i} - v_{O,i}| \quad (12)$$

where $v_{R,i}$ and $v_{O,i}$ represent the i th vector gained from the cross-correlation of the reconstructed particle distributions and the original distributions, respectively. N_V is the total number of vectors. A small value of C indicates a high-quality reconstruction.

As mentioned in Section 2, the acceleration effect of LRDD is inversely proportional to the number of depth layers in the measurement volume (K). According to the definition of K in Eq. (3), the acceleration effect depends on the axial voxel size (V_z) for a certain depth of the measurement volume. Thus, the influence of V_z on the reconstruction, including the reconstruction time, the reconstruction quality and the correlation quality are analysed.

Fig. 4 illustrates the reconstruction time achieved through LRDD and RLD for different V_z . When V_z is 1 μm , 2 μm and 4 μm , LRDD takes 2641 seconds, 685 seconds and 179 seconds, respectively to complete 100 iterations, while RLD takes 25500 seconds, 12117 seconds and 6048 seconds, respectively. This indicates that the reconstruction efficiency of LRDD is 10, 18 and 34 times faster than that of RLD. According to Eq. (3), the values of K with 100 μm depth for the V_z of 1 μm , 2 μm and 4 μm are 101, 51 and 26, respectively. Thus, the acceleration effect of LRDD is inversely proportional to the value of K , which is consistent with the theoretical analysis as discussed in Section 2.

Fig. 5 shows the reconstruction quality Q obtained for LRDD and RLD under different V_z . In general, Q increases with iteration. When V_z increases from 1 μm to 2 μm , Q is unchanged whether for LRDD or RLD. When V_z increases to 4 μm , Q is greatly degraded for both LRDD and RLD. According to the Shannon-Nyquist theorem³⁵, the sampling frequency shall be at least twice the signal frequency. Otherwise, information loss occurs, and the sampling results can be degraded. The axial resolution of the LF microscope through the deconvolution method ranges from 5 to 15 μm when the depth of measurement volume is placed in the region of $30 \mu\text{m} \leq z \leq 130 \mu\text{m}$ ²⁴. To reconstruct the particle distribution in the whole measurement volume without information loss, V_z less than 2.5 μm is necessary. Notably, Q in LRDD becomes lower than that in RLD regardless of V_z after about 30 iterations. The Q is degraded due to the approximation error generated by low-rank decomposition. With the cumulative approximation error after multiple iterations, the reconstructed result obtained through the LRDD deviates from RLD, thereby degrading the Q .

Further to analyse the Q , the typical reconstructed particle distributions under V_z of 2 μm are presented in

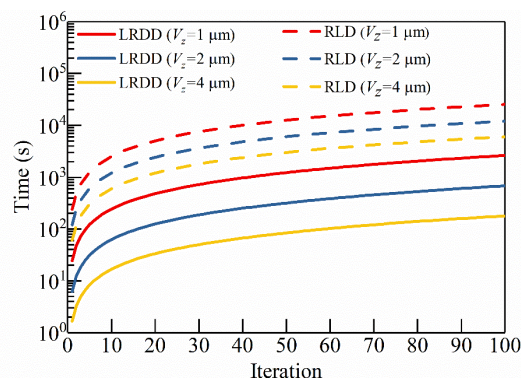


Fig. 4 Reconstruction time achieved through LRDD and RLD for different axial voxel sizes

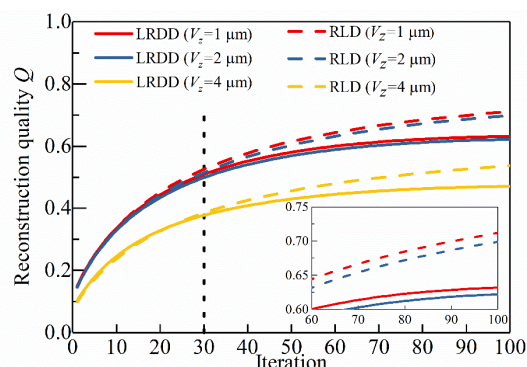


Fig. 5 Reconstruction quality obtained through LRDD and RLD for different axial voxel sizes

Fig. 6(a-d). Compared with the reconstructed particles at the 50th iteration, those at the 100th iteration have a smaller stretch both in LRDD and RLD, which is more consistent with the original particles. This decreased stretch explains the improvement of reconstruction quality. Moreover, Fig. 6(e-f) presents the centerline intensity profiles of the reconstructed particles [blue dotted circle in Fig. 6(a-d)]. The profiles obtained through the LRDD and the RLD both follow Gaussian distribution. The full width at half maxima ($FWHM$) at the 100th iteration is less than that at the 50th iteration [see the width of profile at the dashed line of intensity = 0.5 a.u. in Fig. 6(e-f)], which quantitatively verifies that multiple iterations can reduce the stretch of the reconstructed particle. The line intensity values through LRDD are different from that through RLD for a particular iteration, especially along the z -direction. As there are hundreds of reconstructed particles in the measurement volume, the accumulation of differences in intensity values declined the reconstruction quality. However, in terms of the overall distribution, $FWHM$ and the position of maximum intensity of the centerline intensity profile obtained through the LRDD and RLD are uniform for a particular iteration, indicating that the particle position achieved by the LRDD is consistent with the RLD. The tracer particle is the main factor affecting the cross-correlation accuracy in LF- μ PIV. Therefore, the accuracy of cross-correlation needs to be estimated for the LRDD.

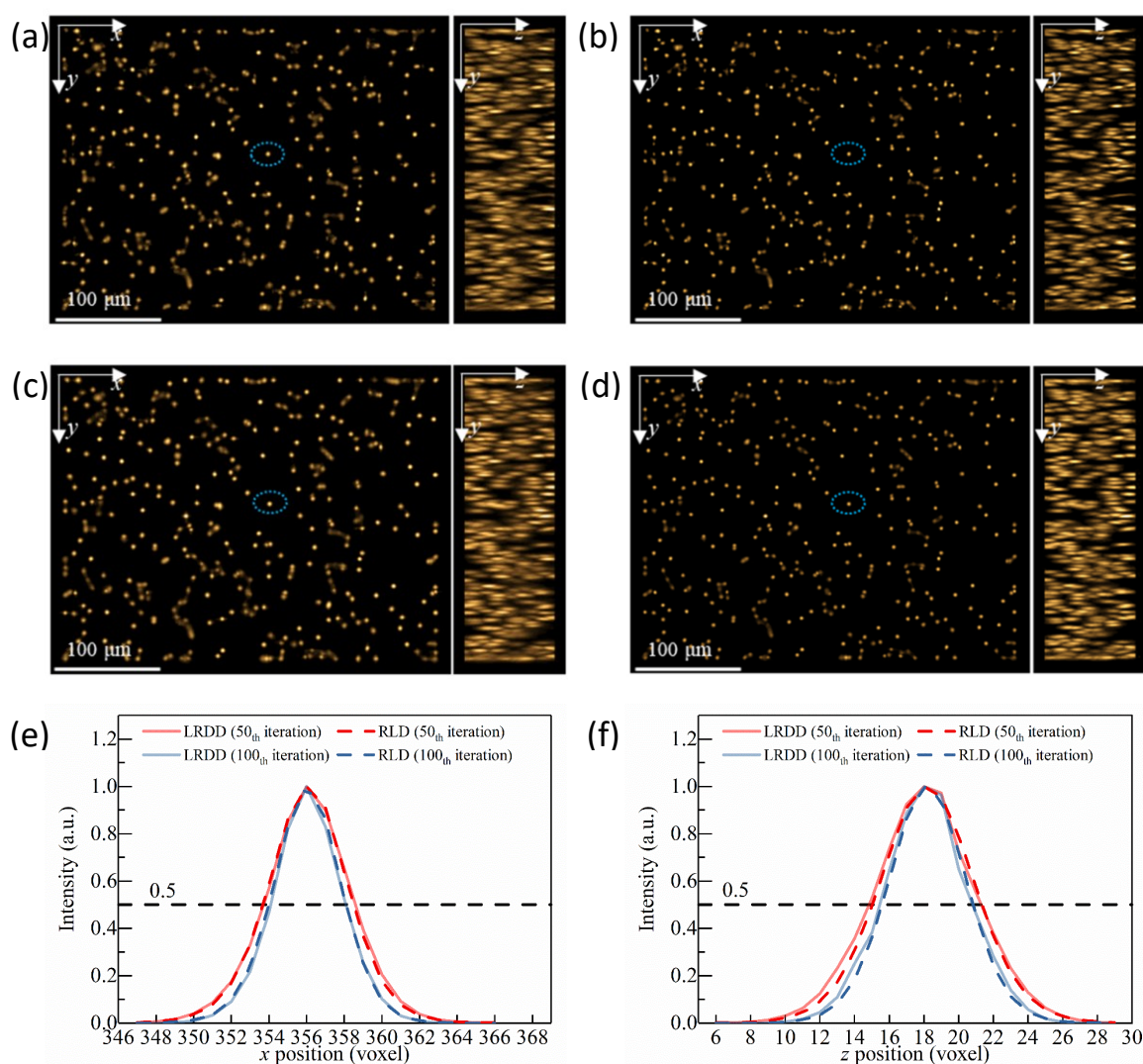


Fig. 6 Particle distributions reconstructed by LRDD and RLD when the axial voxel size is 2 μm: (a) 50th iteration through LRDD; (b) 100th iteration through LRDD; (c) 50th iteration through RLD; (d) 100th iteration through RLD; (e) Centerline intensity profiles of particles along the x-direction; (f) Centerline intensity profiles of particles along the z-direction

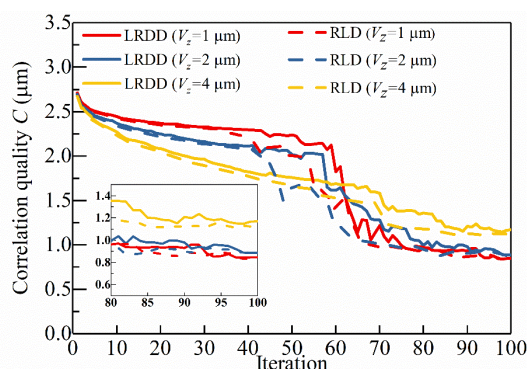


Fig. 7 Correlation quality achieved through LRDD and RLD for different axial voxel sizes

Fig. 7 shows the correlation quality C achieved by the LRDD and RLD for different V_z . As the voxel size is not uniform under different values of V_z , C is characterized in micrometers instead of voxels. The C decreases with iteration, indicating that multiple iterations improve the accuracy of cross-correlation results. When V_z increases from 1 μm to 2 μm, C is the same for both LRDD and RLD after 100 iterations. Further increasing V_z to 4 μm, C is significantly degraded for both LRDD and RLD due to the information loss. Notably, C in LRDD is performed similarly to RLD for a certain V_z , which is different from the variation of the reconstruction quality Q as presented in Fig. 5. The C is affected by the distribution of particle positions. As the entire distribution of particle positions of LRDD is highly like the RLD under the same V_z (Fig. 6), a similar C between the LRDD and the RLD is obtained.

Table 2 Overview of reconstruction performance at the 100th iteration

Algorithm	Axial voxel size V_z / μm	Reconstruction time / s (Acceleration ratio [†])	Reconstruction quality Q	Correlation quality C / μm
RLD	1	25500	0.71	0.83
	2	12117	0.70	0.88
	4	6048	0.54	1.12
LRDD	1	2641 (9.66)	0.63	0.84
	2	685 (17.69)	0.62	0.89
	4	179 (33.79)	0.47	1.17

[†] The acceleration ratio, which is the ratio of the reconstruction time of RLD to that of LRDD under the same axial voxel size, represents the improvement of reconstruction efficiency achieved by the LRDD compared with RLD. A larger acceleration ratio indicates a higher improvement in reconstruction efficiency.

Table 2 summarizes the reconstruction performance at the 100th iteration achieved through the LRDD and RLD. Under different V_z , LRDD is above 9 times faster than the RLD for the volumetric reconstruction. Although increasing V_z decreases the reconstruction time and increases the acceleration ratio, it declines the quality especially when information loss occurs due to the large V_z of 4 μm . Therefore, V_z needs to be determined considering a trade-off between the reconstruction efficiency and the quality. Eventually, V_z of 2 μm is preferred and the reconstruction time of LRDD is nearly 18 times lower than that of RLD. Although the Q drops from 0.70 (RLD) to 0.62 (LRDD), the C slightly changes from 0.88 μm to 0.89 μm . The change of C caused by LRDD is less than 0.01 voxel. Thus, it can be concluded that LRDD can improve the reconstruction efficiency with similar correlation quality of RLD when V_z is 2 μm .

4 Experimental study

Experiments were carried out on a laminar flow at the junction of a Y-shaped microchannel to verify the proposed LRDD, as shown in Fig. 8. The LF- μPIV system consists of a double pulse laser, a syringe pump, a LF microscope (composed of a microscope and a cage LF camera) and a synchronizer. The cage LF camera is assembled by inserting an MLA between the tube lens and the camera through a 1:1 relay lens system. The parameters of the LF microscope are the same as listed in Table 1. The Y-shaped microchannel has a 150 μm width and 100 μm depth with an angle of 90°. The tracer particles are 2 μm fluorescent polystyrene microspheres with a density of 1.05 g/cm^3 . During the experiment, the water injected into the microchannel is seeded with tracer particles at the concentration of 1 ppm (tracer particle per microlens). The flow rates of inlets 1 and 2 are both 14 $\mu\text{L}/\text{min}$, resulting in the bulk flow rate of 28 $\mu\text{L}/\text{min}$ after the junction. The LF microscope captures the LF images of the tracer particles with a two-frame interval of 200 μs . The measurement volume is discretized into voxels with the size of 0.55 $\mu\text{m} \times 0.55 \mu\text{m} \times 2 \mu\text{m}$, resulting in 650 \times 500 \times 51 voxels.

Fig. 9 illustrates the typical captured LF image and corresponding reconstructed tracer particle distribution at the

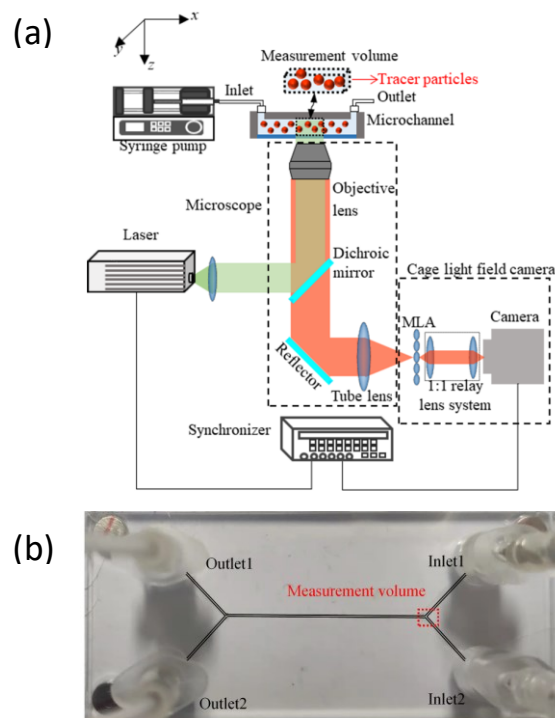


Fig. 8 Schematic of the experimental setup: (a) LF- μPIV system; (b) Y-shaped microchannel

100th iteration. It takes 695 seconds for LRDD to finish the reconstruction with 100 iterations, while RLD takes up to 12859 seconds. Therefore, LRDD is still about 18 times faster than the RLD. The similarity between the two reconstructed tracer particle distributions is acquired through Eq. (11). The Q value of 0.91 indicates that the two reconstructed tracer particle distributions are highly similar, which experimentally confirms the feasibility of the LRDD. The measured velocity field is subsequently calculated by the 3-D cross-correlation algorithm. The interrogation window size is 64 \times 64 \times 10 voxels (35.2 $\mu\text{m} \times 35.2 \mu\text{m} \times 20 \mu\text{m}$) with a 50% overlap. Fig. 10 shows the measured 3-D velocity fields achieved by the LRDD and RLD. The two velocity fields are identical, further validating the feasibility of the LRDD.

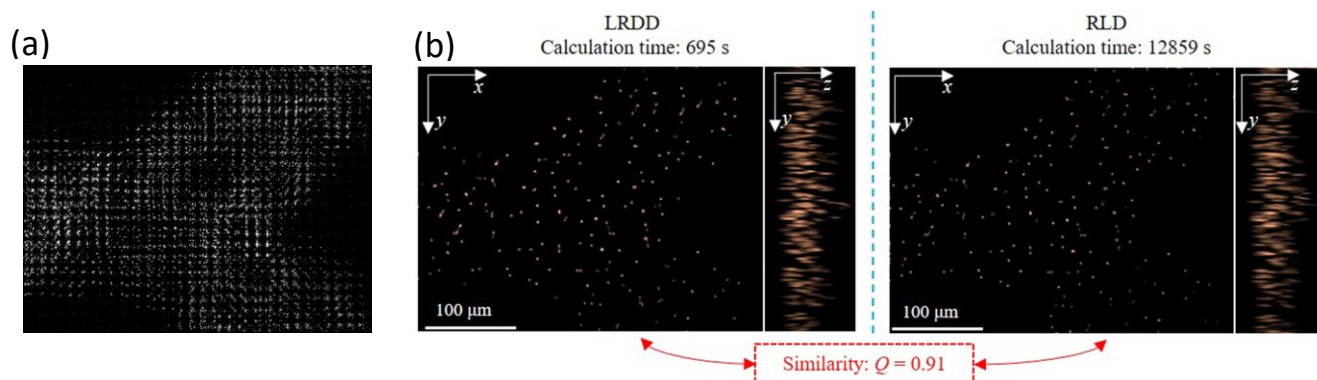


Fig. 9 LF image and reconstructed tracer particle distributions: (a) LF image; (b) Reconstructed tracer particle distributions

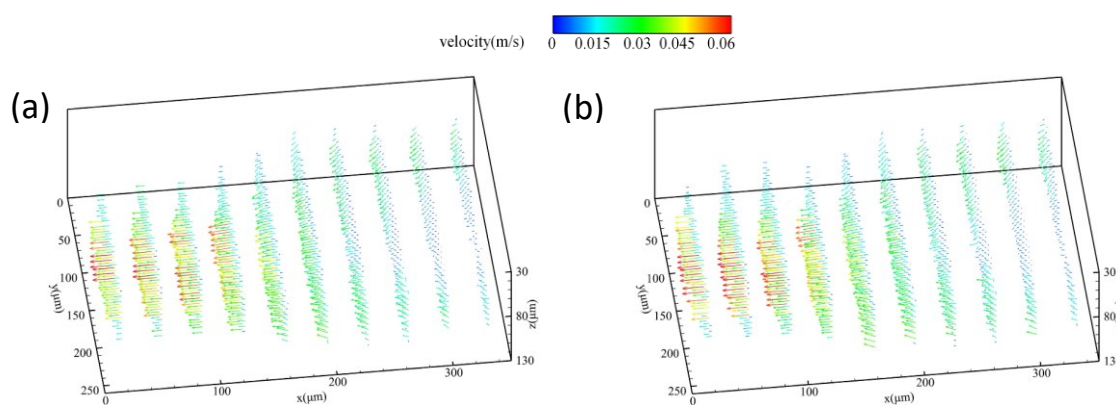


Fig. 10 Measured velocity fields: (a) LRDD and (b) RLD

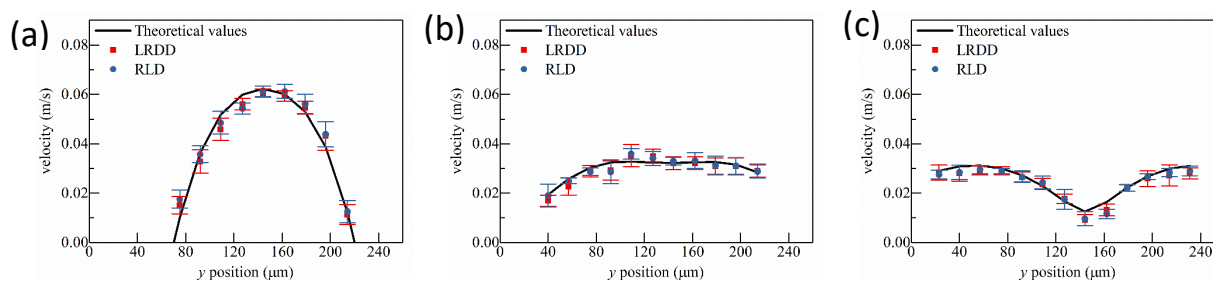


Fig. 11 Comparisons of the measured and theoretical velocity at different x positions over the x - y section of $z = 80 \mu\text{m}$

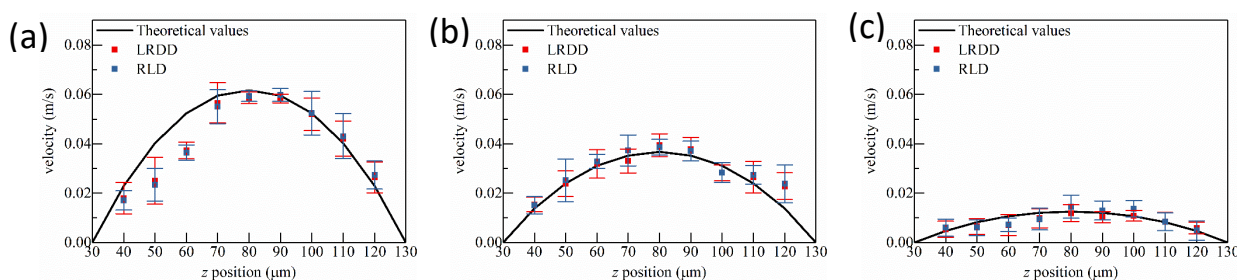


Fig. 12 Comparisons of the measured and theoretical velocity at different x positions over the x - z section of $y = 150 \mu\text{m}$

To evaluate the measurement accuracy, the measured velocity fields achieved by LRDD and RLD are compared with the theoretical values obtained by the computational fluid dynamics (CFD) based on the laminar model²⁶. Figs. 11 and 12 show the comparative results between measured and

theoretical velocity over the x - y section of $z = 80 \mu\text{m}$ and x - z section of $y = 150 \mu\text{m}$, respectively. The results achieved by the LRDD and RLD are consistent with the theoretical values. Over the x - y section, the velocity distribution is a superposition of two parabolas before mixing ($x = 240 \mu\text{m}$). After entering the

junction, the fluids in different inlet channels mix ($x = 140 \mu\text{m}$) and the velocity distribution finally becomes a single parabolic distribution ($x = 40 \mu\text{m}$). This measured mixing process follows the microchannel junction flow characteristic. While over the x - z section of $y = 150 \mu\text{m}$, the velocity remains a single parabola distribution, and the values increase with the increasing distance from the junction wall ($x = 300 \mu\text{m}$), which coincides with the theoretical flow, as shown in Fig. 12.

To quantitatively evaluate the measured velocity fields, the relative deviation v_e is defined as,

$$v_e = \frac{|v_{PIV} - v_{theory}|}{v_{theory}} \times 100\% \quad (13)$$

where v_{PIV} and v_{theory} are the measured velocity by LF- μ PIV and the theoretical value, respectively. The average relative deviations of the LRDD and RLD over the x - y section are 5.85% and 5.80%, respectively, while those over the x - z section are 7.33% and 7.13%, respectively. The relative deviation over the x - z section is higher than that over the x - y section. This can be interpreted that the reconstructed tracer particles having a more considerable stretch along the axial direction. Hence, the measurement accuracy in the axial direction is less than that in the lateral direction. Overall, the bulk flow rates after the junction are estimated as 26.82 $\mu\text{L}/\text{min}$ and 27.02 $\mu\text{L}/\text{min}$ for the LRDD and RLD. They are very close to the experimental flow rate of 28 $\mu\text{L}/\text{min}$. Therefore, a similar accuracy of velocity field measurement between the LRDD and the RLD can be achieved.

5 Conclusions

In this study, a low-rank decomposition-based deconvolution method is proposed to improve the efficiency of the volumetric reconstruction in LF- μ PIV. Numerical simulations are performed on the volumetric reconstruction of tracer particle distribution to analyse the effects of axial voxel size on reconstruction efficiency and quality. Measurements of the microflow in a Y-shaped microchannel were carried out to evaluate the performance of the proposed LRDD. The concluding remarks drawn from this study are summarized as follows.

- The proposed LRDD method optimizes the complex convolution operations in the volumetric reconstruction and thus improves the reconstruction efficiency above 9 times faster than the RLD.
- It has been observed that increasing the axial voxel size can improve reconstruction efficiency but degrade the quality. An appropriate axial voxel size of 2 μm is selected considering the trade-off between the reconstruction efficiency and the quality.
- The LRDD method provides similar accuracy to RLD for the microflow measurement and significantly reduces reconstruction time. It is suggested the LRDD method can be used in the LF- μ PIV for 3-D microflow measurement. Future work will focus on the application of the proposed

LRDD method in different microflows such as convective, secondary and vortex flow.

Conflicts of interest

There are no conflicts to declare.

Acknowledgements

This work was supported by the National Natural Science Foundation of China (No. 51976038, 52006036), Natural Science Foundation of Jiangsu Province, China (No. BK20190366), and Zhishan Scholarship of Southeast University (No. 2242022R40037).

Notes and references

1. H. Ahmed and B. T. Stokke, *Lab Chip*, 2021, **21**, 2232-2243.
2. Y. Wang, X. Zhang, L. Shang and Y. Zhao, *Sci. Bull.*, 2021, **66**, 9-12.
3. Y. Zhang, J. Zhang, Z. Tang and Q. Wu, *Chem. Eng. J.*, 2021, **417**, 129055.
4. S. Watanabe, S. Ohsaki, T. Hanafusa, K. Takada, H. Tanaka, K. Mae and M. T. Miyahara, *Chem. Eng. J.*, 2017, **313**, 724-733.
5. A. Mariotti, C. Galletti, E. Brunazzi and M. Salvetti, *Phys. Fluids*, 2021, **33**, 012008.
6. C. Cierpka and C. Kähler, *J. Vis.*, 2012, **15**, 1-31.
7. M. Levoy, *Computer*, 2006, **39**, 46-55.
8. T. G. Georgiev and A. Lumsdaine, *J Electron Imaging*, 2010, **19**.
9. Q. Qi, M. M. Hossain, B. Zhang, T. Ling and C. Xu, *Meas. Sci. Technol.*, 2019, **30**, 124002.
10. X. Zhu, B. Zhang, J. Li and C. Xu, *Opt. Commun.*, 2020, **462**, 125263.
11. Q. Qi, M. M. Hossain, J.-J. Li, B. Zhang, J. Li and C.-L. Xu, *Opt. Express*, 2021, **29**, 13094-13114.
12. X. Zhu, Z. Wu, J. Li, B. Zhang and C. Xu, *Opt. Lasers Eng.*, 2021, **143**, 106625.
13. X. Zhu, M. M. Hossain, J. Li, B. Zhang and C. Xu, *Measurement*, 2022, **193**, 110982.
14. T. T. Truscott, J. Belden, R. Ni, J. Pendlebury and B. McEwen, *Exp. Fluids*, 2017, **58**, 16.
15. X. Song, M. Gu, L. Cao, Z. Tang and C. Xu, *IEEE Sens. J.*, 2019, **19**, 9806-9817.
16. M. Levoy, R. Ng, A. Adams, M. Footer and M. Horowitz, *ACM Trans. Graph.*, 2006, **25**, 924-934.
17. J. S. Park, C. K. Choi and K. D. Kihm, *Exp. Fluids*, 2004, **37**, 105-119.
18. J. Sheng, E. Malkiel and J. Katz, *Appl. Opt.*, 2006, **45**, 3893-3901.
19. P. Song, H. Verinaz-Jadan, C. L. Howe, A. J. Foust and P. L. Dragotti, *IEEE Signal Process. Mag.*, 2022, **39**, 58-72.
20. N. Wagner, F. Beuttenmueller, N. Norlin, J. Gierten, J. C. Boffi, J. Wittbrodt, M. Weigert, L. Hufnagel, R. Prevedel and A. Kreshuk, *Nat. Methods*, 2021, **18**, 557-563.
21. Z. Wang, L. Zhu, H. Zhang, G. Li, C. Yi, Y. Li, Y. Yang, Y. Ding, M. Zhen and S. Gao, *Nat. Methods*, 2021, **18**, 551-556.
22. L. Hong and L. P. Chamorro, *Lab Chip*, 2022, **22**, 964-971.
23. M. Broxton, L. Grosenick, S. Yang, N. Cohen, A. Andalman, K. Deisseroth and M. Levoy, *Opt. Express*, 2013, **21**, 25418-25439.

24. X. Song, J. Li, M. Gu and C. Xu, *Opt. Commun.*, 2020, **475**, 126302.
25. Z. Lu, J. Wu, H. Qiao, Y. Zhou, T. Yan, Z. Zhou, X. Zhang, J. Fan and Q. Dai, *Opt. Express*, 2019, **27**, 18131-18145.
26. M. Gu, J. Li and C. Xu, *Exp. Fluids*, 2022, **63**, 1-15.
27. P. Sarder and A. Nehorai, *IEEE Signal Process. Mag.*, 2006, **23**, 32-45.
28. A. Sironi, B. Tekin, R. Rigamonti, V. Lepetit and P. Fua, *IEEE Trans. Pattern Anal. Mach. Intell.*, 2014, **37**, 94-106.
29. S. Lin, R. Ji, C. Chen, D. Tao and J. Luo, *IEEE Trans. Pattern Anal. Mach. Intell.*, 2018, **41**, 2889-2905.
30. W. Ren, J. Zhang, L. Ma, J. Pan, X. Cao, W. Zuo, W. Liu and M.-H. Yang, *Proc. Adv. Neural Inf. Process. Syst.*, 2018, **31**.
31. R. Prevedel, Y.-G. Yoon, M. Hoffmann, N. Pak, G. Wetzstein, S. Kato, T. Schrödel, R. Raskar, M. Zimmer and E. S. Boyden, *Nat. Methods*, 2014, **11**, 727-730.
32. M. Eberhart, *Opt. Express*, 2021, **29**, 24129-24143.
33. G. E. Elsinga, F. Scarano, B. Wieneke and B. W. van Oudheusden, *Exp. Fluids*, 2006, **41**, 933-947.
34. D. Schanz, S. Gesemann, A. Schröder, B. Wieneke and M. Novara, *Meas. Sci. Technol.*, 2012, **24**, 024009.
35. C. E. Shannon, *The Bell Syst. Tech. J.*, 1948, **27**, 379-423.